Relating 3D Geometry and Photoelectrochemical Activity of WO_3-loaded n-Si Nanowires: Design Rules for Photoelectrodes

Yihui Zhao [a], Shashank Balasubramanyam [b], Ageeth. A. Bol [b], Anja Bieberle-Hütter [a*]

[a] *Electrochemical Materials and Interfaces (EMI), Dutch Institute for Fundamental Energy Research (DIFFER), 5600 HH Eindhoven, The Netherlands*

[b] *Plasma and Materials Processing (PMP), Department of Applied Physics, Eindhoven University of Technology (TU/e), 5600 MB Eindhoven, The Netherlands*

[*] Corresponding author, E-mail: a.bieberle@differ.nl, Postal address: PO Box 6336, NL-5600 HH Eindhoven, the Netherlands

Keywords: photoelectrochemical water splitting, nanostructure geometry, activity, Si etching, ALD WO_3 film

Abstract

Nanostructured electrodes for photoelectrochemical (PEC) applications, such as water splitting, have rather low photocurrent density regarding their highly enlarged surface area compared to plain electrodes. This demands for further understanding of the relation between the 3D geometry and the PEC activity. To this end, we fabricate WO_3/Si nanowire array photoanodes with various nanowire lengths (1.3 µm, 2.7 µm, 3.2 µm and 3.8 µm) and different WO_3 thicknesses (10 nm, 30 nm and 50 nm) using wet chemical etching for nanostructuring of Si and atomic layer deposition for the deposition of WO_3. It is found that by increasing the etching time, the nanowires become longer and the top surface area decreases. The photocurrent density first increases and then decreases with increasing Si etching time. This behaviour can be explained by different and opposite effects regarding absorption, geometry and materials specific properties. Particularly, the decrease of the photocurrent density can be due to: First, the longer the nanowires the heavier the recombination of the photogenerated carriers. Second, the long-time Si etching results in a loss of top part of the nanowire arrays. Because of shadowing, the WO_3 located at the top part of the nanowires is more effective than that at the bottom part for the WO_3/Si nanowire arrays and therefore the photocurrent is decreased. It reveals a trade-off between the top part surface area and the length of the nanowires. This study contributes to a better understand of the relation between the geometry of nanostructures and the performance of PEC electrodes.

1 Introduction

Growing environmental concerns and an increasing energy demand drive the search for new, sustainable sources of energy. Converting solar energy to chemical fuels is considered as a potential pathway for renewable energy utilization[1–3]. Hydrogen production from photo-electrochemical (PEC) water splitting has received continually attention since the first discovery by Fujishima and Honda[4]. PEC water splitting process involves two half-cell reactions, the hydrogen evolution reaction (HER) and the oxygen evolution reaction (OER). OER, which occurs at the photoanode, is more complex because it requires multiple bond rearrangements that involve the removal of four electrons and two protons from two H_2O molecules[5,6]. Among all the photoanode materials, metal oxides, such as TiO_2, WO_3, Fe_2O_3, and $BiVO_4$, have been studied elaborately for catalyzing OER reactions in PEC water splitting because of their suitable band edges positions and chemical stability[7–12]. To supply sufficient energy (including overpotential) for splitting water, the band gaps of metal oxides tend to be substantial (≥ 1.9), which limits their absorption of solar light[13].

To achieve more efficient use of the capable light, the nanostructured photoelectrodes with porous morphology are used to enhance the light absorption by decreasing light reflection and increasing transmission path of light[13–16]. In addition, compared with the film and bulk counterparts, nanostructured materials have much larger electrode/electrolyte interface area and shorter diffusion distance for minority carriers, which promote the separation and transfer of photogenerated carriers[17,18]. According to these reasons, various nanostructured metal oxide photoanodes have been designed and synthesized to enhance the PEC performance, like TiO_2 nanotubes[19,20], WO_3 nanoneedles[21], nanoflowers[22] and Fe_2O_3 nanoflakes[23,24], etc. Furthermore, nanostructured heterojunctions have been developed, such as nanostructured $WO_3/BiVO_4$[25,26], WO_3/ZnO[27], and Fe_2O_3/ZnO[27].

In addition, n-Si nanowires have been used as substrate for metal oxide films to create a tandem structure PEC device. The optimum band structures of Si addresses the deficiencies of the metal oxides in light harvesting[28]. Moreover, the metal oxide/n-Si heterojunction works as a Z-scheme and creates photovoltage to enhance the charge transport property[29–31]. As reported in the literature, TiO_2/n-Si nanowires showed a photocurrent density of ~0.25 mA/cm^2, which is about 2.5 times higher than planar TiO_2/n-Si[14]. The fabricated Fe_2O_3/n-Si in Mayer et al.[31] exhibited a current density of ~ 0.9 mA/cm^2 at 1.23 V vs RHE, which was 5 times higher than the corresponding planar electrode[31]. A hierarchically nanostructured WO_3/Si achieved up to 0.14 mA at 1.23 V vs RHE, which is a three times enhancement compared to the planar design. Moreover, when the spacing of the nanostructures in the photoelectrode is on the scale of the wavelength, photonic effects should be taken into consideration. Studies aiming at optimizing the overall light absorption have demonstrated the importance of a joint optimization of the nanostructure size, shape, and filling ratio.[32–34]

Besides the studies mentioned above, PEC electrodes from metal oxide/Si nanowires can also address the question of spatial and functional decoupling of the geometry and the catalytic activity. This has not been studied sufficiently in the literature so fa and is the main aim of the current study. Therefore, we fabricate in this study Si nanowires by chemical etching and prepare WO_3/Si nanowires photoanodes by atomic layer deposition (ALD) of WO_3 films to

evaluate the effects of the geometry of the nanostructures on the PEC performance. WO_3 is selected as the functional layer due to its high electron mobility (~12 $cm^2V^{-1}s^{-1}$ at RT) and suitable band-gap (2.6-2.9 eV)[35,36]. The geometries of WO_3/Si nanowire arrays are varied regarding the nanowire length, total surface area, and top surface area by controlling the Si chemical etching time (20 min, 30 min, 40 min, 50 min).

This research shows systematically the relation between the geometry of nanostructured electrodes and its PEC performance. The complexity in this relation is discussed in detail in this study and shows that several performance determining factors interfere. Such analysis guides towards designing high performing nanostructure photoelectrodes.

2 Results

2.1 Morphology, structure, and optical properties

Figure 1 shows the morphology of the Si nanowires and ALD WO_3 coated Si nanowires. As shown in the optical photographs in Figure 1a, the Si wafer changes from mirror-like to black after chemical etching. This is because the created nanowire structure minimizes the light reflection by trapping light inside the surface channels[37]. Figure 1b and c show the SEM images of the Si nanowires fabricated by chemical etching for 50 min. The bright clusters in the top view image (Figure 1b) illustrate the top surface of the Si nanowires. The cross-sectional views (Figure 1c) show that the nanowire arrays are in a vertical direction and have a homogenous length of about 3.7 μm. Figure S1 shows the SEM images of Si nanowire arrays fabricated by chemical etching for different times, namely 20 min, 30 min, 40 min and 50 min. From the top view images, it can be seen that the density of the bright cluster decreases with increasing etching time, which reflects a decreased top surface area. The length of the nanowire arrays increases with increasing etching time. For different etching times, the nanowires are 1.3 μm (20 min), 2.7 μm (30 min), 3.2 μm (40 min) and 3.8 μm (50 min) long, error bar was derived from several samples as to be around 10%. Figure 1 c, d and e show the morphology of the Si nanowires coated with ALD WO_3. Comparing with the plain Si nanowires, the WO_3/Si nanowire arrays show more rounded cluster structure from the top view (Figure 1d) and the diameters of the nanowires also increase (Figure 1e). The FIB-cut cross-section of the WO_3/Si nanowire arrays in Figure 1f demonstrates that the Si nanowires are fully covered by WO_3 (bright layer in Figure 1f). Figure S2 shows the SEM images of WO_3/Si nanowires fabricated with different Si etching time and different WO_3 thickness. The top surface area of WO_3/Si nanowires increases with the WO_3 thickness and decreases with the increasing Si etching time. Figure S3 shows the grazing incidence X-ray diffraction (GIXRD) spectra of WO_3/Si nanowire arrays. The diffraction peaks of the WO_3 agree well with monoclinic WO_3 (JCPDS No. 83-0950) indicating that monoclinic WO_3 crystalline strucuture is obtained after annealing in Ar. The chemical states of the ALD WO_3 films have been investigated by X-ray photoelectron spectroscopy (XPS) in our previous work[38]. The WO_3 films were fabricated with the same method and annealed under the same condition; mainly W^{6+} and oxygen were identified at the surface which confirms the formation of WO_3.

The band gap of the ALD WO_3 films is ~3.0 eV, which has been calculated with Tauc plots in our previous work.[38] The light reflectance data is shown in the Supporting Information in

Fig. S4. Comparing with the planar electrode, the nanowires array structures decrease light reflectance. For 20 min Si etching with different WO_3 thickness, the light reflectance increases with the reduced WO_3 film thickness.

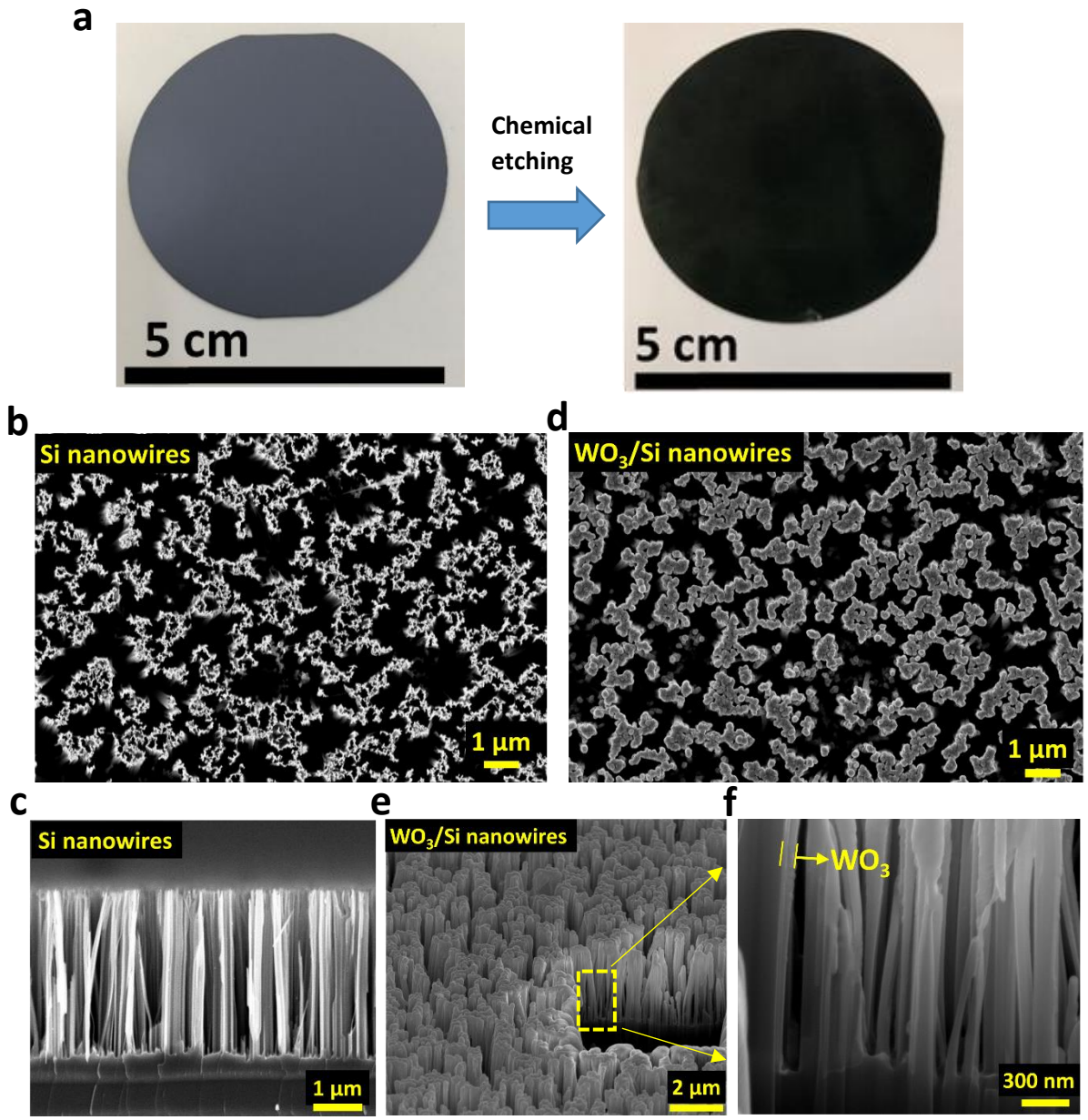

Figure 1. (a) Optical photographs of Si wafer before (left) and after (right) chemical etching. (b-f) Scanning electron microscope (SEM) images of (b) top view of Si nanowires (50 min etching), (c) cross-section of Si nanowires (50 min etching), (d) top view of 50 nm WO_3 coated Si (WO_3/Si) nanowires (50 min etching Si) by ALD, (e) FIB-cut of WO_3/Si nanowires, (f) enlargement of dotted box in (d).

2.2 Photo-electrochemistry

The PEC activity of the WO_3/Si nanowire array electrodes are evaluated by the photocurrents as a function of the applied potential (0.3 - 1.7 V vs RHE), which were measured in 0.5 M H_2SO_4 under continuous AM 1.5 illumination. Figure 2 shows the photocurrent densities obtained from the WO_3/Si nanowires with different Si etching time and thicknesses

of the ALD WO_3 films. Among all the electrodes, the highest photocurrent density is obtained from the WO_3/Si nanowire arrays with 40 min Si etching time and 50 nm WO_3 coating. A photocurrent density of about 0.41 mA/cm^2 at 1.23 V vs RHE was achieved. This is about 4 times higher than that for planar WO_3/Si electrodes. The data is comparable to the WO_3 nanowire and microwire photoanodes reported previously[39,40].

Comparing the WO_3/Si electrodes with different WO_3 thickness (Figure 2 a-c), it is found that the photocurrent density increases with increased WO_3 films thickness, which is due to more photons harvested by the WO_3, and therefore more photogenerated carriers contributing to the PEC reactions. Further increasing the thickness in a certain range can further increase the performance. However, if continually increase the thickness, the performance will decrease. One reason is that the recombination rate of the photogenerated electron-hole pairs will increase due to the limitation of the charge diffusion length (~150 nm) within WO_3.[41] The second reason is the thicker WO_3 film would close the nanostructure, which results in a decrease of the surface area. Thirdly, the closed nanostructure can result in a higher light reflectance, which would also decrease the PEC performance. Besides, with thicker WO_3 films, the difference in photocurrent density becomes more significant for electrodes with different Si etching time. In addition, for each thickness of WO_3, the PEC performance does not keep increasing as the Si etching time increased, even though the longer etching time resulted in an increased nanowires length. To clarify the tendency of the changing photocurrent densities, Figure 2d summarizes the photocurrent densities at 1.23 V vs RHE of all electrodes from Figure 2a-c. It shows that, for each thickness of WO_3 film, the photocurrent density at 1.23 V vs RHE increases first and then decreases as the Si etching time increases. Besides, the highest photocurrent density obtained from each WO_3 thickness falls at different Si etching time. Respectively, for 10 nm WO_3, the highest photocurrent is from 20 min etching Si; for 30 nm WO_3, the highest photocurrent is from 30 min etching Si; for 50 nm WO_3, the highest photocurrent is from 40 min etching Si (green dash circles in Figure 2d). This variation indicates a coupling effect of the amount of the catalyst and the geometry of the nanowire array.

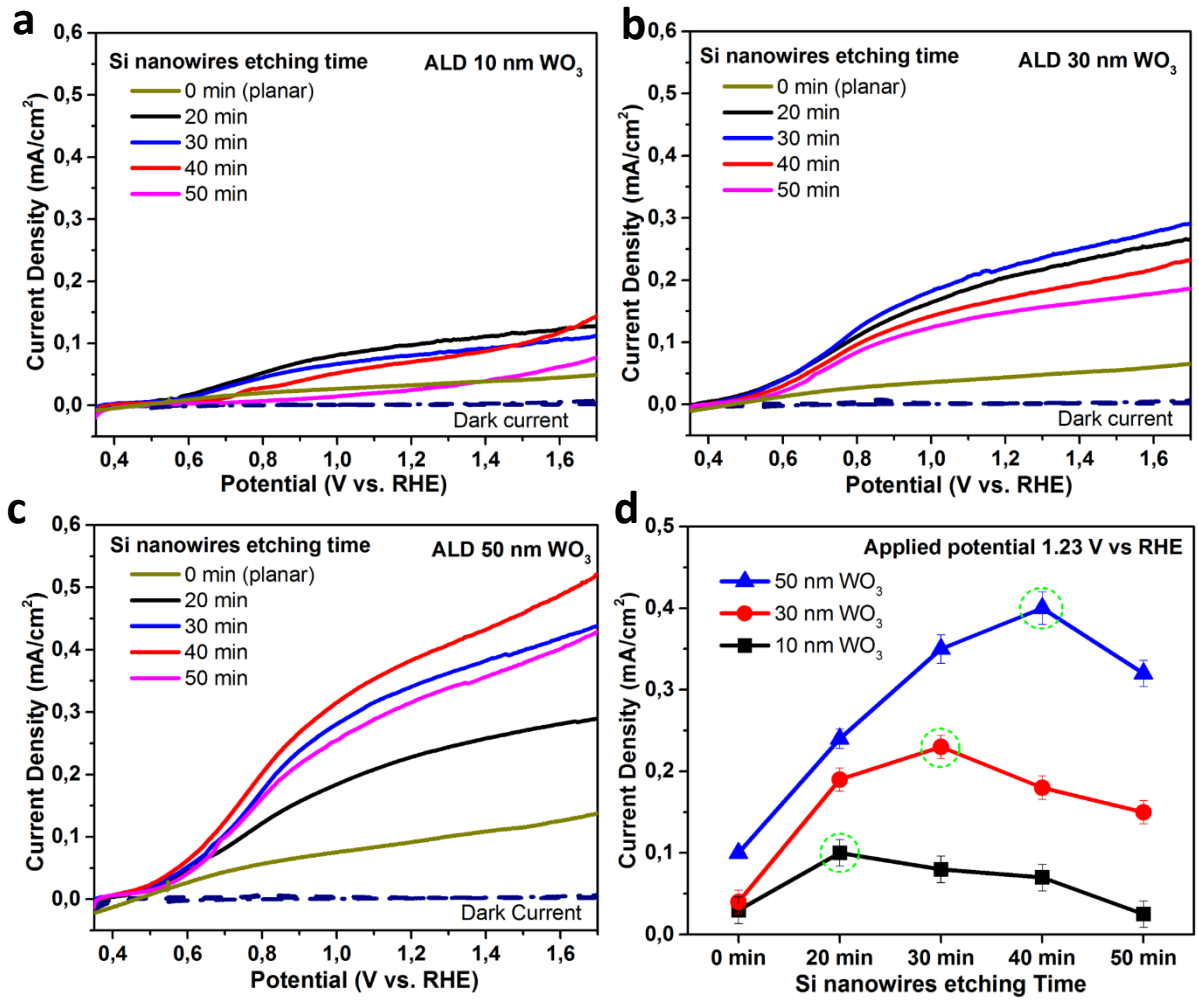

Figure 2. Photocurrent density vs applied potential curves of WO_3/Si nanowires with different etching time of the Si nanowires and different thickness of WO_3 films: (a) 10 nm, (b) 30 nm and (c) 50 nm (light intensity: 100 mW cm^{-2}; electrolyte: 0.5 M H_2SO_4, the dark current curves are all overlapping). (d) Photocurrent densities at 1.23 V vs RHE of WO_3/Si nanowires with different etching time Si nanowires and different thickness of WO_3 films. The error bars denote the standard deviation of two different repetitive measurements in two different samples.

To investigate the effect of geometry on the activity further, we carry out a quantitative analysis on the relation between photocurrent densities and 3D geometry of the WO_3/Si nanowire arrays. We define several parameters to describe the geometry of the nanowire arrays as shown in Figure 3: the top surface area, S_T; the wall surface area, S_W; the bottom surface area, S_B; the length of the contour of the top surface, L_C; and the length of the nanowires, L_W. S_T and L_C are determined from the SEM images using the commercial software (Gwyddion) for scanning image analysis. We derived the following equation for calculating the total surface area of the WO_3/Si nanowire arrays:

$$S_{Total} = S_W + S_T + S_B = (L_C \times L_W) + S_T + S_B \quad (1)$$

Figure 4 a-c illustrate the relation between the photocurrent density and the total surface area of the WO_3/Si nanowire arrays. Due to the increased nanowires length L_W, the total surface areas (blue curves) increase with the Si etching time for all three different thicknesses of WO_3

films. However, the photocurrent density (black curves) does not show a consistent increase with increasing total surface area. For three different thicknesses of WO_3 films, the photocurrent densities first increases and then decreases with increasing Si etching time. Particularly, the inflection points, which is the maximum value of the photocurrent density curves, are different for the three different WO_3 thicknesses, i.e. the inflection point appears at a longer etching time when the WO_3 thickness is thicker.

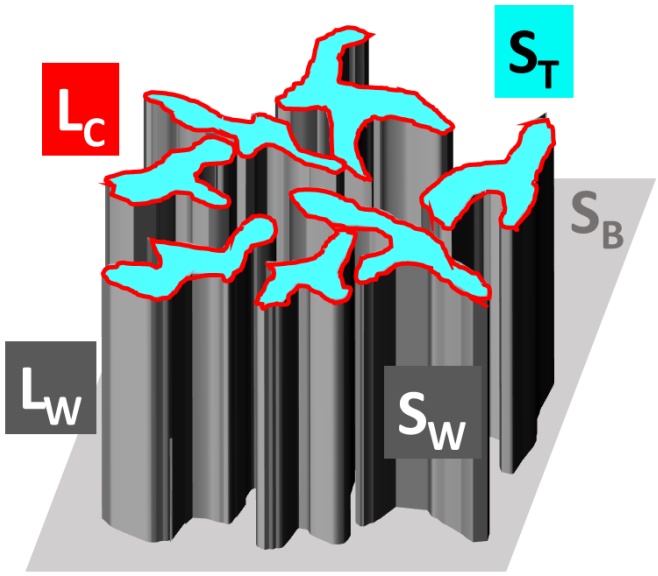

Figure 3. Sketch of the geometry of the WO_3/Si nanowires (S_T: top surface area; L_C: length of the contour of the top surface; L_W: length of the nanowires; S_W: wall surface area; S_B: bottom surface area.)

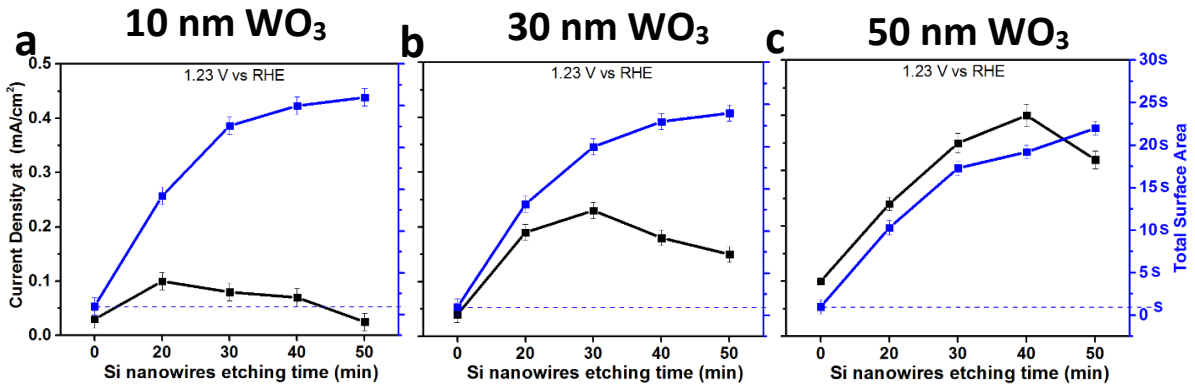

Figure 4. The total surface areas (blue) and photocurrent densities at 1.23 V vs RHE (black) of WO_3/Si nanowires electrodes with different Si nanowires etching time (0 min, 20 min, 30 min, 40 min, 50 min) and different WO_3 thickness: (a) 10 nm, (b) 30 nm and (c) 50 nm. The error bars denote the standard deviation of two different repetitive measurements in two different samples.

3 Discussion

Necessary conditions for PEC reactions to take place are an active photoelectrode with a lot of catalytic sites and optimal light illumination and management. For the nanowire WO_3/Si photoelectrodes, the larger surface area of WO_3 due to the nanostructure and conformal ALD deposition provide more catalytic sites than plannar electrodes. The reduced reflectance, which

is due to internal reflection and absorption in the structure, results in better light harvesting than the plannar electrode (Figure S4). Moreover, the spacing between nanowires is on the scale of the wavelength, hence, photonic-crystal effects could also enhance the light harvesting[32–34]. These factors can explain the increasing part of photocurrent density as the Si etching time increases (Figure 4). However, longer Si etching times can also result in negative effects: First, due to a higher recombination rate of photogenerated carriers at the surface compared to in the bulk of Si, the enlarged surface area can result in more recombinations. Second, more defects in Si due to longer etching time can also cause more recombinations of photogenerated carriers. These factors result in a slower increase of the photocurrent density as a function of the Si etching time. Furthermore, due to the grown structure of the nanowire array, shadowing causes lower PEC activity for the WO_3 located at the lower part than the top part of the nanowires.[42] A sketch in Figure 5 illustrates the relation between the active surface area of the WO_3/Si nanowire array and the Si etching time. Longer etching time results in a loss of Si volume and surface area in the top part of the nanowire array (Figure S1) and therefore less WO_3 at the top part (Figure S2). When the etching time further increases, the increased lower part with lower activity can not compensate for the loss of the top surface area with higher acivity, and thus results in a decrease of photocurrent density. This is the reason that inflection points appear at the photocurrent density curves. In brief, for WO_3/Si nanowire arrays with longer Si etching time, a lack of highly active WO_3 at the top part limits the continous growth of the photocurrent densities. This is corresponding with the inflection points of the photocurrent density curves at different thicknesses of WO_3 (Figure 2d and Figure 4). The thicker WO_3 film delays the inflection point of the photocurrent density as the function of Si etching time, because a thicker WO_3 film provides more catalytic material and results in a larger top surface area with high catalytic activity, which makes up the loss of the top surface area caused by longer Si etching times.

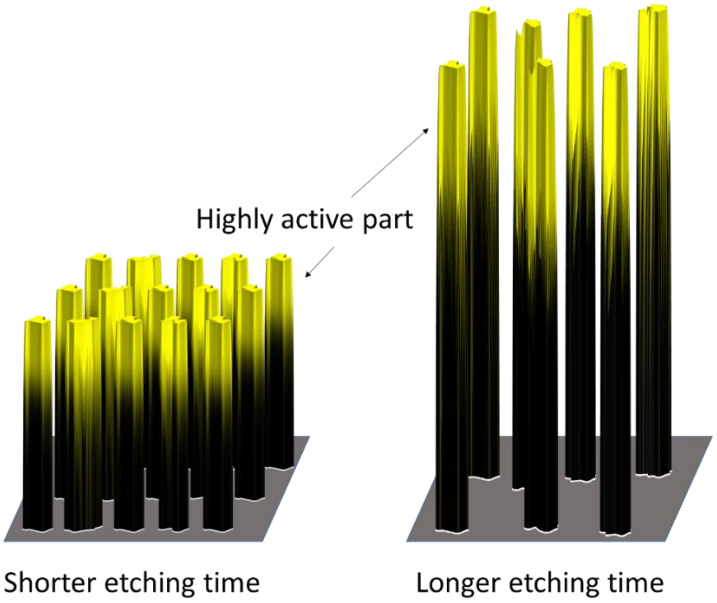

Figure 5. Sketch of the active surface area of WO_3/Si nanowire array with shorter and longer Si etching time.

To guide towards design rules for high performing nanowire array photoelectrodes, we summarize the effect of the top surface area and the length of the WO_3/Si nanowires on the PEC activity, i.e. the photocurrent density of all electrodes at 1.23 V vs RHE. The data is summarized in the contour plot in Figure 6. To obtain optimal PEC performance, a trade-off has to be made between the top surface area and the length of the nanowires. At the upper of the contour plot according to the large top surface area, the photocurrent density is limited by the higher light reflection, which has been proven by the optical results of the WO_3/Si nanowire arrays (Figure S4). On the contrary, the longer nanowires can reduce the light reflection, but if the top surface area is low (lower right corner of Figure 6), the photocurrent density is still limited, which is due to the loss of high active top surface area. Therefore, the best PEC perpormance is obtained for WO_3/Si electrodes with relative long nanowires and also the largest top surface area possible.

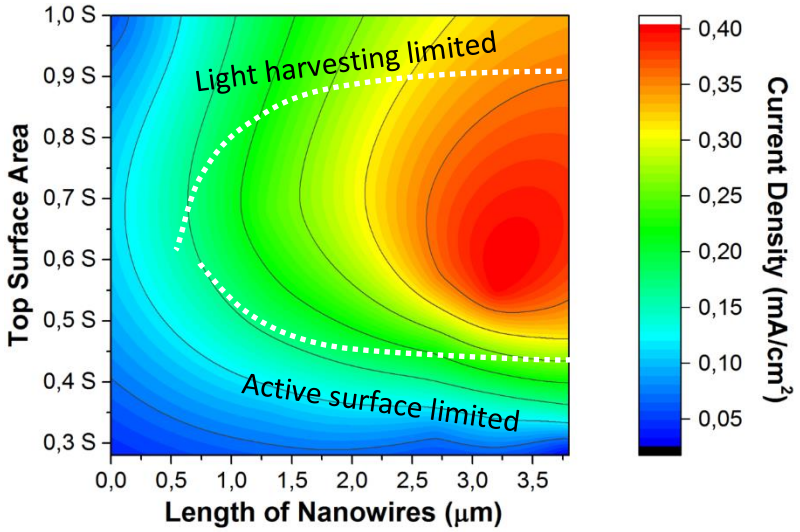

Figure 6. Contour plot of current density at 1.23 V vs RHE as a function of top surface area and nanowire length of WO_3/Si nanowire photoelectrodes.

4 Conclusion

WO_3/Si nanowire array photoanodes with various nanowire lengths (1.3 µm, 2.7 µm, 3.2 µm and 3.8 µm) and different WO_3 thicknesses (10 nm, 30 nm and 50 nm) are fabricated using wet chemical etching for nanostructuring of Si and atomic layer deposition for the deposition of WO_3. The best performance is obtained by the WO_3/Si nanowire array with 40 min chemical etching coated with 50 nm ALD WO_3 film. It resulted in a photocurrent density of 0.41 mA/cm^2 at 1.23 V vs RHE, which is 4 times enhancement compared to a planar WO_3/Si electrode. With a longer Si etching time, it is predicted that the PEC performance is enhanced because of an extended nanowire length, i.e. an enlarged total surface area. However, the photocurrent density decreases with the increasing nanowire length at a certain Si etching time. This can be attributed to multiple reasons: First, the longer nanowires cause more recombination of the photogenerated carriers. Second, due to the grown structure of the nanowires, shadowing causes lower PEC activity for the WO_3 located at the lower part than the top part of the nanowires. Long time Si etching results in an increased total surface area but also a loss of top surface area of the nanowire arrays. The increased surface area, i.e. from the lower part of the nanowires,

has relatively lower activity, which cannot compensate for the loss of the top surface area with relatively higher activity, and thus results in a decrease of photocurrent density. These results reveal a trade-off between the top surface area and the length of the nanowires.

This systematic study contributes to a better understanding of the relation between the geometry of nanostructures and their performance as PEC electrodes. A nanowire geometry provides in principle effective means to enhance the PEC performance; however, high aspect ratios do not always bring the advantage that is expected due to long distance to the back contact and low conductivity. A new perspective for the future could be to integrate well-conducting paths to make the entire nanowire active.

5 Experimental section

Fabrication of Si nanowires array

The Si wafers (n-doped, <100> orientation, resistivity 1-10 Ω cm, 280 μm-thick, single side polished, University Wafer) were cleaned sequentially in an ultrasonic bath of isopropanol and distilled (DI) water each for 20 min. Then, the Si nanowire arrays were fabricated by chemical etching, similarly as described in Peng et al.[43] Briefly after cleaning, the wafer was immersed in a mixed solution of 4.4 M HF and 0.02 M $AgNO_3$ at room temperature. The etching time determines the length of the nanowires. In this work, we used different etching times (20 min, 30 min, 40 min and 50 min) to obtain varied lengths of the nanowires (1.3 μm, 2.7 μm, 3.2 μm and 3.8 μm, accordingly). After etching, the wafers were rinsed with DI water and then immersed in concentrated HNO_3 for 15 min to remove Ag nanoparticle residue. Finally, the wafer was rinsed with DI water and dried by N_2 blowing.

WO_3 film deposition

A FlexAL atomic layer deposition (ALD) reactor from Oxford Instruments, equipped with an inductively coupled plasma (ICP) source, was used to deposit WO_3. The metalorganic precursor $(^tBuN)_2(Me_2N)_2W$ (99% purity, Sigma Aldrich) was used as the tungsten source and O_2 plasma was used as the co-reactant. The deposition rate was 0.025 Å/s. The thickness of the WO_3 films were controlled by the number of ALD cycles. In this work, WO_3 films with three different thicknesses (10 nm, 30 nm, and 50 nm) were prepared to study the effect of thickness. The main parameters of the ALD process are listed in Table 1. The details of the plasma enhanced ALD process are described in detail in ref.[38,44].

Table 1: ALD process parameters for WO_3 deposition.

Parameter	Value
Base pressure	$<10^{-6}$ mbar
Table temperature	300°C
O_2 plasma power	250 W

Precursor dosing	3 s
Co-reactant O_2 plasma exposure	3 s

After deposition, all samples were annealed at 450°C in Ar for 1 h with a ramping rate of 5°C/min using a tubular furnace with a quartz tube (Carbolite Gero). The Ar gas flow was started 30 min prior to annealing to guarantee a complete Ar atmosphere.

Characterizations

The morphologies of the micropillar array electrodes were investigated by a field emission scanning electron microscope (SEM) (Zeiss Sigma, Germany) with an in-lens detector and 5 kV accelerating voltage. Cross-sectional SEM samples were prepared using a focused ion beam (FIB) (FEI, the Netherlands).

PEC measurements

A three-electrode PEC cell with a quartz window was used to measure the PEC performance at room temperature. Simulated sunlight illumination was performed by an AM 1.5 class A solar simulator (LCS 100, Oriel Instruments) using a 100 W Xe lamp with a calibrated illumination intensity of 100 mW cm^{-2} at the sample position. The light source was calibrated with a calibrated reference cell and meter (Newport, model 91150 V). For the assembly of the WO_3/n-Si nanowires array photoanodes (working electrodes), a small area of fresh Si was exposed on the NW array surface by scraping away the NWs with a blade and roughing the Si with a diamond pen. For ohmic contact to the n-Si (backside of the electrodes), a drop of Ga/In eutectic (Sigma Aldrich) was used for contact between the Si and a copper wire. Then, the devices were encapsulated in epoxy (Loctite EA 9492) resulting in an exposed micropillar arrays area of about 0.2 cm^2. The exact geometrical area of the exposed electrode surface was determined by calibrated digital images and ImageJ. A coiled Pt wire (0.8 mm in thickness) was used as the counter electrode and an Ag/AgCl/Sat. KCl electrode (XR 300, Radiometer Analytical) was used as reference electrode. An aqueous solution of 0.5 M H_2SO_4 (pH ~0.3) was used as electrolyte. The potential of the electrode was controlled with a BioLogic SP-150 potentiostat. All potentials reported in this study are given versus reversible hydrogen electrode (RHE) through the relation[2]

$$\Phi_{RHE} = \Phi_{Ag/AgCl} + \Phi^{o}_{Ag/AgCl\ vs\ RHE} + 0.059 \times pH \quad (2)$$

with $\Phi^{o}_{Ag/AgCl}$ is 0.197 V versus RHE at 25°C. Linear sweep voltammetry (LSV) measurements were performed at potentials between 0.3 V and 1.7 V versus RHE at a scan rate of 10 mV s^{-1}.

For each processing condition, two samples were prepared. Each sample was measured for 3 times. The contour plot in Figure 6 was created with 12 sets of data, i.e. 3 different thicknesses and 4 different nanowire lengths.

ASSOCIATED CONTENT

Supporting Information Available: **SEM images, GIXRD patterns, UV-vis light absorbance spectra**

Acknowledgements

Y. Zhao and A. Bieberle-Hütter acknowledge the financial support from the China Scholarship Council (CSC) and from NWO [FOM program nr. 147 "CO_2 neutral fuels"], respectively. The authors thank Nanolab at TU/e for access to SEM and Dr. Erwin Zoethout (DIFFER) for performing the FIB cutting and cross-sectional SEM. The authors acknowledge Dr. Biplab Patra (AMOLF) for help with UV-VIS measurements and prof. Erik Garnett (AMOLF) for discussion of the manuscript.

Reference

(1) Walter, M. G.; Warren, E. L.; Mckone, J. R.; Boettcher, S. W.; Mi, Q.; Santori, E. A.; Lewis, N. S. Solar Water Splitting Cells. *Chem. Rev.* **2010**, *110*, 6446–6473. https://doi.org/10.1021/cr1002326.

(2) Tuller, H. L. *Photoelectrochemical Hydrogen Production*; van de Krol, R., Grätzel, M., Eds.; Electronic Materials: Science & Technology; Springer US: Boston, MA, 2012; Vol. 102. https://doi.org/10.1007/978-1-4614-1380-6.

(3) Nathan S. Lewis. Research Opportunities to Advance Solar Energy Utilization. *Science* **2016**, *351* (6271), aad1920. https://doi.org/10.1126/science.aad1920.22.

(4) Fujishima, A.; Honda, K. Electrochemical Photolysis of Water at a Semiconductor Electrode. *Nature* **1972**, *238* (5358), 37–38. https://doi.org/10.1038/238037a0.

(5) Sivula, K.; van de Krol, R. Semiconducting Materials for Photoelectrochemical Energy Conversion. *Nat. Rev. Mater.* **2016**, *1*, 15010. https://doi.org/10.1038/natrevmats.2015.10.

(6) Tang, J.; Durrant, J. R.; Klug, D. R. Mechanism of Photocatalytic Water Splitting in TiO_2 Reaction of Water with Photoholes, Importance of Charge Carrier Dynamics, and Evidence for Four-Hole Chemistry. *J. Am. Chem. Soc.* **2008**, *130* (42), 13885–13891. https://doi.org/10.1021/ja8034637.

(7) Somorjai, G. A.; Bratlie, K. M.; Montano, M. O.; Park, J. Y. Dynamics of Surface Catalyzed Reactions; the Roles of Surface Defects, Surface Diffusion, and Hot Electrons. *J. Phys. Chem. B* **2006**, *110* (40), 20014–20022. https://doi.org/10.1021/jp062569d.

(8) Liu, R.; Lin, Y.; Chou, L.-Y.; Sheehan, S. W.; He, W.; Zhang, F.; Hou, H. J. M.; Wang, D. Water Splitting by Tungsten Oxide Prepared by Atomic Layer Deposition and Decorated with an Oxygen-Evolving Catalyst. *Angew. Chemie Int. Ed.* **2011**, *50* (2), 499–502. https://doi.org/10.1002/anie.201004801.

(9) Hong, S. J.; Lee, S.; Jang, J. S.; Lee, J. S. Heterojunction $BiVO_4/WO_3$ Electrodes for Enhanced Photoactivity of Water Oxidation. *Energy Environ. Sci.* **2011**, *4* (5), 1781–1787. https://doi.org/10.1039/c0ee00743a.

(10) Janáky, C.; Rajeshwar, K.; De Tacconi, N. R.; Chanmanee, W.; Huda, M. N. Tungsten-Based Oxide Semiconductors for Solar Hydrogen Generation. *Catal. Today* **2013**, *199* (1), 53–64. https://doi.org/10.1016/j.cattod.2012.07.020.

(11) Monllor–Satoca, D.; Bärtsch, M.; Fàbrega, C.; Genç, A.; Hilaire, S.; Andreu, T.; Arbiol, J.; Niederberger, M.; Morante, J. R. What Do You Do, Titanium? Insight into the Role of Titanium Oxide as Water Oxidation Promoter in Hematite-Based Photoanodes. *Energy Environ. Sci.* **2015**, *8* (iv), 3242–3254. https://doi.org/10.1039/C5EE01679G.

(12) Lopes, T.; Andrade, L.; Le Formal, F.; Grätzel, M.; Sivula, K.; Mendes, A. Hematite

Photoelectrodes for Water Splitting: Evaluation of the Role of Film Thickness by Impedance Spectroscopy. *Phys. Chem. Chem. Phys.* **2014**, *16* (31), 16515–16523. https://doi.org/10.1039/C3CP55473B.

(13) van de Krol, R.; Liang, Y.; Schoonman, J. Solar Hydrogen Production with Nanostructured Metal Oxides. *J. Mater. Chem.* **2008**, *18* (20), 2311–2320. https://doi.org/10.1039/B718969A.

(14) Hwang, Y. J.; Boukai, A.; Yang, P. High Density N-Si/n-TiO_2 Core/Shell Nanowire Arrays with Enhanced Photoactivity. *Nano Lett.* **2009**, *9* (1), 410–415. https://doi.org/10.1021/nl8032763.

(15) Sivula, K.; Le Formal, F.; Grätzel, M. Solar Water Splitting: Progress Using Hematite (α-Fe_2O_3) Photoelectrodes. *ChemSusChem* **2011**, *4* (4), 432–449. https://doi.org/10.1002/cssc.201000416.

(16) Le Formal, F.; Pendlebury, S. R.; Cornuz, M.; Tilley, S. D.; Grätzel, M.; Durrant, J. R. Back Electron-Hole Recombination in Hematite Photoanodes for Water Splitting. *J. Am. Chem. Soc.* **2014**, *136* (6), 2564–2574. https://doi.org/10.1021/ja412058x.

(17) Kuang, Y.; Jia, Q.; Nishiyama, H.; Yamada, T.; Kudo, A.; Domen, K. A Front-Illuminated Nanostructured Transparent $BiVO_4$ Photoanode for >2% Efficient Water Splitting. *Adv. Energy Mater.* **2016**, *6* (2), 1501645. https://doi.org/10.1002/aenm.201501645.

(18) Narkeviciute, I.; Chakthranont, P.; MacKus, A. J. M.; Hahn, C.; Pinaud, B. A.; Bent, S. F.; Jaramillo, T. F. Tandem Core-Shell Si-Ta_3N_5 Photoanodes for Photoelectrochemical Water Splitting. *Nano Lett.* **2016**, *16* (12), 7565–7572. https://doi.org/10.1021/acs.nanolett.6b03408.

(19) Kang, Q.; Cao, J.; Zhang, Y.; Liu, L.; Xu, H.; Ye, J. Reduced TiO_2 Nanotube Arrays for Photoelectrochemical Water Splitting. *J. Mater. Chem. A* **2013**, *1* (18), 5766–5774. https://doi.org/10.1039/c3ta10689f.

(20) Kuang, S.; Yang, L.; Luo, S.; Cai, Q. Fabrication, Characterization and Photoelectrochemical Properties of Fe_2O_3 Modified TiO_2 Nanotube Arrays. *Appl. Surf. Sci.* **2009**, *255* (16), 7385–7388. https://doi.org/10.1016/j.apsusc.2009.04.005.

(21) Corby, S.; Franca, L.; Selim, S.; Sachs, M.; Blackman, C.; Kafizas, A.; Durrant, J. R. Water Oxidation and Electron Extraction Kinetics in Nanostructured Tungsten Trioxide Photoanodes. *J. Am. Chem. Soc.* **2018**, *140* (47), 16168–16177. https://doi.org/10.1021/jacs.8b08852.

(22) Wang, N.; Wang, D.; Li, M.; Shi, J.; Li, C. Photoelectrochemical Water Oxidation on Photoanodes Fabricated with Hexagonal Nanoflower and Nanoblock WO_3. *Nanoscale* **2014**, *6* (4), 2061–2066. https://doi.org/10.1039/c3nr05601e.

(23) Wang, L.; Lee, C. Y.; Mazare, A.; Lee, K.; Müller, J.; Spiecker, E.; Schmuki, P. Enhancing the Water Splitting Efficiency of Sn-Doped Hematite Nanoflakes by Flame Annealing. *Chem. Eur. J.* **2014**, *20* (1), 77–82. https://doi.org/10.1002/chem.201303427.

(24) Rajendran, R.; Yaakob, Z.; Pudukudy, M.; Rahaman, M. S. A.; Sopian, K. Photoelectrochemical Water Splitting Performance of Vertically Aligned Hematite Nanoflakes Deposited on FTO by a Hydrothermal Method. *J. Alloys Compd.* **2014**, *608*, 207–212. https://doi.org/10.1016/j.jallcom.2014.04.105.

(25) Pihosh, Y.; Turkevych, I.; Mawatari, K.; Asai, T.; Hisatomi, T.; Uemura, J.; Tosa, M.; Shimamura, K.; Kubota, J.; Domen, K.; Kitamori, T. Nanostructured WO_3/$BiVO_4$ Photoanodes for Efficient Photoelectrochemical Water Splitting. *Small* **2014**, *10* (18), 3692–3699. https://doi.org/10.1002/smll.201400276.

(26) Zeng, Q.; Li, J.; Li, L.; Bai, J.; Xia, L.; Zhou, B. Synthesis of WO3/BiVO4 Photoanode Using a Reaction of Bismuth Nitrate with Peroxovanadate on WO3 Film for Efficient Photoelectrocatalytic Water Splitting and Organic Pollutant Degradation. *Appl. Catal. B Environ.* **2017**, *217*, 21–29. https://doi.org/10.1016/j.apcatb.2017.05.072.

(27) Barreca, D.; Carraro, G.; Gasparotto, A.; Maccato, C.; Altantzis, T.; Sada, C.; Kaunisto, K.; Ruoko, T. P.; Bals, S. Vapor Phase Fabrication of Nanoheterostructures Based on ZnO for Photoelectrochemical Water Splitting. *Adv. Mater. Interfaces* **2017**, *4* (18), 1–9. https://doi.org/10.1002/admi.201700161.

(28) Noh, S. Y.; Sun, K.; Choi, C.; Niu, M.; Yang, M.; Xu, K.; Jin, S.; Wang, D. Branched TiO_2/Si Nanostructures for Enhanced Photoelectrochemical Water Splitting. *Nano Energy* **2013**, *2*, 351–360. https://doi.org/10.1016/j.nanoen.2012.10.010.

(29) Zhao, Y.; Brocks, G.; Genuit, H.; Lavrijsen, R.; Verheijen, M. A.; Bieberle-Hütter, A. Boosting

the Performance of WO_3/n-Si Heterostructures for Photoelectrochemical Water Splitting : From the Role of Si to Interface Engineering. *Adv. Energy Mater.* **2019**, 1900940. https://doi.org/10.1002/aenm.201900940.

(30) Hwang, Y. J.; Boukai, A.; Yang, P. High Density N-Si/n-TiO2Core/Shell Nanowire Arrays with Enhanced Photoactivity. *Nano Lett.* **2009**, *9*, 410–415. https://doi.org/10.1021/nl8032763.

(31) Mayer, M. T.; Du, C.; Wang, D. Hematite/Si Nanowire Dual-Absorber System for Photoelectrochemical Water Splitting at Low Applied Potentials. *J. Am. Chem. Soc.* **2012**, *134* (30), 12406–12409. https://doi.org/10.1021/ja3051734.

(32) Kim, S. J.; Thomann, I.; Park, J.; Kang, J.; Vasudev, A.; Brongersma, M. L. Light Trapping for Solar Fuel Generation with Mie Resonances Light Trapping for Solar Fuel Generation with Mie Resonances. *Nnao Lett.* **2014**, *14*, 1446–1452. https://doi.org/10.1021/nl404575e.

(33) Garnett, E.; Yang, P. Light Trapping in Silicon Nanowire Solar Cells. *Nano Lett.* **2010**, *10* (3), 1082–1087. https://doi.org/10.1021/nl100161z.

(34) Brongersma, M. L.; Cui, Y.; Fan, S. Light Management for Photovoltaics Using High-Index Nanostructures. *Nat. Mater.* **2014**, *13* (5), 451–460. https://doi.org/10.1038/nmat3921.

(35) Zhu, T.; Chong, M. N.; Chan, E. S. Nanostructured Tungsten Trioxide Thin Films Synthesized for Photoelectrocatalytic Water Oxidation: A Review. *ChemSusChem* **2014**, *7* (11), 2974–2997. https://doi.org/10.1002/cssc.201402089.

(36) Bignozzi, C. A.; Caramori, S.; Cristino, V.; Argazzi, R.; Meda, L.; Tacca, A. Nanostructured Photoelectrodes Based on WO_3: Applications to Photooxidation of Aqueous Electrolytes. *Chem. Soc. Rev.* **2013**, *42* (42), 2228–2246. https://doi.org/10.1039/c2cs35373c.

(37) Yu, Y.; Zhang, Z.; Yin, X.; Kvit, A.; Liao, Q.; Kang, Z.; Yan, X.; Zhang, Y.; Wang, X. Enhanced Photoelectrochemical Efficiency and Stability Using a Conformal TiO_2 Film on a Black Silicon Photoanode. *Nat. Energy* **2017**, *2*, 17045. https://doi.org/10.1038/nenergy.2017.45.

(38) Zhao, Y.; Balasubramanyam, S.; Sinha, R.; Lavrijsen, R.; Verheijen, M. A.; Bol, A. A.; Bieberle-Hütter, A. Physical and Chemical Defects in WO_3 Thin Films and Their Impact on Photoelectrochemical Water Splitting. *ACS Appl. Energy Mater.* **2018**, *1* (11), 5887–5895. https://doi.org/10.1021/acsaem.8b00849.

(39) Su, J.; Guo, L.; Bao, N.; Grimes, C. A. Nanostructured WO_3/$BiVO_4$ Heterojunction Films for Efficient Photoelectrochemical Water Splitting. *Nano Lett.* **2011**, *11* (5), 1928–1933. https://doi.org/10.1021/nl2000743.

(40) Shaner, M. R.; Fountaine, K. T.; Ardo, S.; Coridan, R. H.; Atwater, H. a.; Lewis, N. S. Photoelectrochemistry of Core–Shell Tandem Junction n–p^+-Si/n-WO_3 Microwire Array Photoelectrodes. *Energy Environ. Sci.* **2014**, *7* (2), 779. https://doi.org/10.1039/c3ee43048k.

(41) Valerini, D.; Hernández, S.; Di Benedetto, F.; Russo, N.; Saracco, G.; Rizzo, A. Sputtered WO_3 Films for Water Splitting Applications. *Mater. Sci. Semicond. Process.* **2016**, *42*, 150–154. https://doi.org/10.1016/j.mssp.2015.09.013.

(42) Zhao, Y.; Westerik, P.; Santbergen, R.; Zoethout, E.; Gardeniers, H.; Bieberle-Hütter, A. From Geometry to Activity: A Quantitative Analysis of WO3/Si Micropillar Arrays for Photoelectrochemical Water Splitting. *Adv. Funct. Mater.* **2020**, *1909157*, 1–10. https://doi.org/10.1002/adfm.201909157.

(43) Peng, K.; Xu, Y.; Wu, Y.; Yan, Y.; Lee, S. T.; Zhu, J. Aligned Single-Crystalline Si Nanowire Arrays for Photovoltaic Applications. *Small* **2005**, *1* (11), 1062–1067. https://doi.org/10.1002/smll.200500137.

(44) Balasubramanyam, S.; Sharma, A.; Vandalon, V.; Knoops, H. C. M.; Erwin Kessels, W. M. M.; Bol, A. A. Plasma-Enhanced Atomic Layer Deposition of Tungsten Oxide Thin Films Using $(^tBuN)_2(Me_2N)_2W$ and O_2 Plasma. *J. Vac. Sci. Technol. A Vacuum, Surfaces Film.* **2018**, *36* (1), 01B103. https://doi.org/10.1116/1.4986202.

Table of Contents

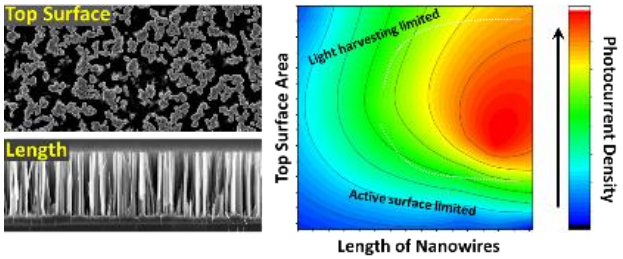

For Table of Contents Only